

UNIVERSIDAD DE LOS ANDES

MASTER THESIS

The effect of gas bulk rotation on the morphology of the Lyman α line

Author:

Juan Nicolas Garavito Camargo

Supervisor:

Dr. Jaime E. ForeroRomero

*A thesis submitted in fulfilment of the requirements
for the degree of Master in Phycis*

in the

Astronomy group
Physics Department

April 2015

UNIVERSIDAD DE LOS ANDES

Abstract

Faculty of Science
Physics Department

Master in Phycis

Effect of the gas bulk rotation on the morphology of the Lyman α line

by Juan Nicolas GARAVITO CAMARGO

We present results of radiative transfer calculations to measure the impact of gas bulk rotation on the morphology of the Lyman α emission line in distant galaxies. We model a galaxy as a sphere with an homogeneous mixture of dust and hydrogen at a constant temperature. These spheres undergo solid-body rotation with maximum velocities in the range $0-300 \text{ km s}^{-1}$ and neutral hydrogen optical depths in the range $\tau_{\text{H}} = 10^5-10^7$. We consider two types of source distributions in the sphere: central and homogeneous. Our main result is that rotation introduces a dependence of the line morphology with viewing angle and rotational velocity. Observations with a line of sight parallel to the rotation axis yield line morphologies similar to the static case. For lines of sight perpendicular to the rotation axis both the intensity at the line center and the line width increase with rotational velocity. Along the same line of sight, the line becomes single peaked at rotational velocities close to half the line width in the static case. Notably, we find that rotation does not induce any spatial anisotropy in the integrated line flux, the escape fraction or the average number of scatterings. This is because Lyman α scattering through a rotating solid-body proceeds identical as in the static case. The only difference is the doppler shift from the different regions in the sphere that move with respect to the observer. This allows us to derive an analytic approximation for the viewing-angle dependence of the emerging spectrum, as a function of rotational velocity.

Acknowledgements

To do ...

Contents

Abstract	i
Acknowledgements	ii
Contents	iii
List of Figures	v
List of Tables	vii
1 Introduction	1
2 Models of bulk gas rotation	3
2.0.1 Detailed Implementation of Rotation	3
2.0.2 Brief Description of the Radiative Transfer Codes	4
2.0.3 Grid of Simulated Galaxies	6
3 Results	9
3.0.4 Line Morphology	9
3.0.5 Integrated Line Intensity	10
3.0.6 Full Width at Half Maximum	11
3.0.7 Line Maxima	13
3.0.8 Dusty Clouds: Escape Fraction	13
3.0.9 Average Number of Scatterings	14
4 Discussion	16
4.0.10 Towards an analytical description	16
4.0.11 Impact on the interpretation of simulated and observational data .	17
5 Conclusions	19
A Analytic Expression for the Lyα Spectrum emerging from Rotating Cloud	21

Bibliography

24

List of Figures

2.1	Geometry of the gas distribution. The angular velocity vector is parallel to the unit vector \hat{k} . In order to describe the departures from spherical symmetry we use the polar angle θ formed by the direction of the outgoing photons with respect to the z -axis. We define the variable $\mu \equiv \cos \theta$ to report to present our results. Computing the spectra for photons in a narrow range of μ is equivalent to having a line-of-sight oriented in that direction.	4
2.2	2D histogram showing the number of photons that escape with frequency x forming an angle θ (parametrized as $ \cos \theta $) with the rotation axis. The rotational velocity (0, 100, 200, 300 km s ⁻¹) increases from left to right and the optical depth (10 ⁵ , 10 ⁶ , 10 ⁷) from top to bottom. The Ly α photons are initialized at the center of the sphere. Two main results can be read from this figure. First, the line morphology depends on the viewing angle. Second, the line can become single peaked for high rotational velocities.	5
2.3	Same as Fig. 2.2 for Ly α photons initialized homogeneously throughout the sphere.	6
2.4	Shape of the Ly α line for different maximum rotational velocities for a LoS perpendicular to the rotation axis ($ \mu \sim 0$). The continuous (dashed) line represents the central (homogeneous) source distributions. The continuous thin line represents the intrinsic homogeneous spectrum. The panels follow the same distribution as in Figs 2.2 and 2.3.	7
2.5	Shape of the Ly α line for different maximum rotational velocities for a LoS perpendicular to the rotation axis ($ \mu \sim 1$). The continuous (dashed) line represents the central (homogeneous) source distributions. The continuous thin line represent the intrinsic homogeneous spectrum. The panels follow the same distribution as in Figs 2.2 and 2.3.	8
3.1	Integrated flux distribution as a function of the viewing angle as parametrized by μ . Continuous (dashed) correspond to central (homogeneous) source distribution. The models correspond to an optical depth of $\tau_H = 10^5$ and rotational velocities of 100 km s ⁻¹ , 200 km s ⁻¹ and 300 km s ⁻¹ . The distributions are flat in the range of models probed in this work, meaning that the integrated flux for all viewing angles is the same.	10
3.2	FWHM for the non-dusty models as a function of the viewing angle parametrized by $ \cos \theta $. Continuous (dashed) lines correspond to central (homogeneous) source distributions. The general trend is of an decreasing line width as the line of sight becomes parallel to the rotation axis.	11

3.3	FWHM for the non-dusty models as a function of rotational velocity V_{\max} for observers located perpendicular to the rotation axis. The left panel shows the results in velocity units while the right panel normalizes the data by the FWHM in the static case. Continuous (dashed) lines correspond to central (homogeneous) source distributions. The straight lines represent the fit to the data using the expression in Eq. (3.2).	12
3.4	Position of the line maxima as a function of maximum rotational velocity V_{\max} . Continuous (dashed) lines correspond to central (homogeneous) source distributions. A value of $x_{\max} = 0$ indicates that line becomes single peaked.	12
3.5	2D histogram of the logarithm of the average number of scatterings as function of μ (left) and the maximum rotational velocity V_{\max} (right). The left panel shows the behaviour for $\tau = 10^5$ and $V_{\max} = 300 \text{ km s}^{-1}$ as a function of $ \cos \theta $, the color indicates the number of photons per bin. In the right panel the continuous (dashed) lines represent the results for the central (homogeneous) model. The independence of N_{scatt} with μ and V_{\max} is present in all models.	14
4.1	Comparison of the Monte Carlo results against the analytic solution. The left panel explores the results of different velocities. The right panel presents the results for two different observers: paralel and perpendicular to the rotational axis, $\mu = 1$ and $\mu = 0$ respectively.	17

List of Tables

2.1	Summary of Physical Parameters of our Monte Carlo Simulations.	7
3.1	Escape fraction values for all dusty models.	13

To my parents: Vilma & Edgar

Chapter 1

Introduction

The detection of strong Ly α emission lines has become an essential method in extragalactic astronomy to find distant star-forming galaxies [1–8]. The galaxies detected using this method receive the name of Ly α emitters (LAEs). A detailed examination of this galaxy population has diverse implications for galaxy formation, reionization and the large scale structure of the Universe. Attempts to fully exploit the physical information included in the Ly α line require an understanding of all the physical factors involved in shaping the line. Due to the resonant nature of this line, these physical factors notably include temperature, density and bulk velocity field of the neutral Hydrogen in the emitting galaxy and its surroundings. A basic understanding of the quantitative behavior of the Ly α line has been reached through analytic studies in the case of a static configurations, such as uniform slabs [9–11] and uniform spheres [12]. Analytic studies of configurations including some kind of bulk flow only include the case of a sphere with a Hubble like expansion flow [13]. A more detailed quantitative description of the Ly α line has been reached through Monte Carlo (MC) simulations [9, 14, 15]. In the last two decades these studies have become popular due to the availability of computing power. Early into the 21st century, the first studies focused on homogeneous and static media [16–18]. Later on, the effects of clumpy media [19] and expanding/contracting shell/spherical geometries started to be studied [12, 20, 21]. For a recent review, we refer the interested reader to Dijkstra [22]. Similar codes have applied these results to semi-analytic models of galaxy formation [23, 24] and results of large hydrodynamic simulations [25–27]. Recently, Monte Carlo codes have also been applied to the results of high resolution hydrodynamic simulations of individual galaxies [28–31]. Meanwhile, recent developments have been focused on the systematic study of clumpy outflows [32] and anisotropic velocity configurations [33]. The recent studies of galaxies in hydrodynamic simulations [28–31] have all shown systematic variations in the Ly α line with the viewing angle. These variations are a complex superposition of anisotropic density

configurations (i.e. edge-on vs. face-on view of a galaxy), the inflows observed by gas cooling and the outflows included in the supernova feedback process of the simulation. These bulk flows physically correspond to the circumgalactic and intergalactic medium (CGM and IGM). These effects are starting to be studied in simplified configurations that vary the density and wind characteristics [33, 34]. However, in all these efforts the effect of rotation, which is an ubiquitous feature in galaxies, has not been systematically studied. The processing of the Ly α photons in a rotating interstellar medium (ISM) must have some kind of impact in the Ly α line morphology. Performing that study is the main goal of this thesis. We investigate for the first time the impact of rotation on the morphology of the Ly α line. We focus on a simplified system: a spherical gas cloud with homogeneous density and solid body rotation, to study the line morphology and the escape fraction in the presence of dust. We base our work on two independent Monte Carlo based radiative transfer codes presented in [25] and [32]. This thesis is structured as follows: In §2 we present the implementation of bulk rotation into the Monte Carlo codes, paying special attention to coordinate definitions. We also present a short review of how the Ly α radiative transfer codes work and list the different physical parameters in the simulated grid of models. In §3 we present the results of the simulations, with special detail to quantities that show a clear evolution as a function of the sphere rotational velocity. In §4 we discuss the implications of our results. In the last section we present our conclusions. The Appendix presents the derivation of an analytic expression to interpret the main trends observed in the Monte Carlo simulations. In this work we express a photon's frequency in terms of the dimensionless variable $x \equiv (\nu - \nu_a)/\Delta\nu_D$, where $\nu_a = 2.46 \times 10^{15}$ Hz is the Ly α resonance frequency, $\Delta\nu_D \equiv \nu_a \sqrt{2kT/m_p c^2} \equiv \nu_a v_{\text{th}}/c$ is the Doppler broadening of the line which depends on the neutral gas temperature T or equivalently the thermal velocity v_{th} of the atoms. We also use the parameter a to define the relative line width as $a = \Delta\nu_\alpha/2\Delta\nu_D$, where $\Delta\nu_\alpha$ is the intrinsic linewidth. For the temperature $T = 10^4$ K used in our radiative transfer calculations the thermal velocity is $v_{\text{th}} = 12.8 \text{ km s}^{-1}$.

Chapter 2

Models of bulk gas rotation

Describing the kinematics of gas rotation in all generality is a complex task, specially at high redshift where there is still missing a thorough observational account of rotation in galaxies beyond $z > 1.0$. Even at low redshifts there is a great variation in the shape of the rotation curve as observed in HI emission as a function of the distance to the galaxy center. However there are two recurrent features. First, in the central galactic region the velocity increases proportional to the radius, following a solid rotation behavior. Second, beyond a certain radius the rotation curve tends to flatten. An ab-initio description of such realistic rotation curves in simulations depends on having access to the dynamic evolution of all mass components in the galaxy: stars, gas and dark matter. Such level of realism is extremely complex to achieve, specially if one wants to get a systematic description based on statistics of simulated objects. Following the tradition of studies of Ly α emitting systems, we implement a model with simplified geometry. We assume that the gas is homogeneously distributed in a sphere that rotates as a solid body with constant angular velocity. This simple model will contain only one free parameter: the linear velocity at the sphere's surface, V_{max} .

2.0.1 Detailed Implementation of Rotation

In the Monte Carlo code we define a Cartesian coordinate system to describe the position of each photon. The origin of this system coincides with the center of the sphere and the rotation axis is defined to be z -axis. With this choice, the components of the gas bulk velocity field, $\vec{v} = v_x\hat{i} + v_y\hat{j} + v_z\hat{k}$, can be written as

$$v_x = -\frac{y}{R}V_{\text{max}}, \quad (2.1)$$

$$v_y = \frac{x}{R}V_{\text{max}}, \quad (2.2)$$

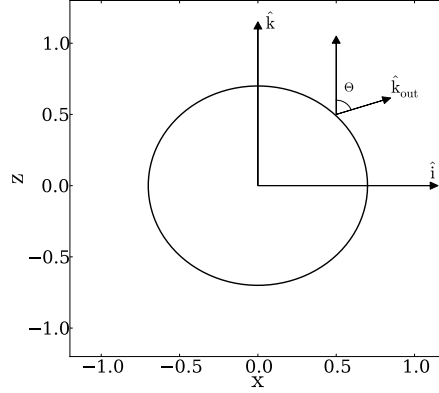


FIGURE 2.1: Geometry of the gas distribution. The angular velocity vector is parallel to the unit vector \hat{k} . In order to describe the departures from spherical symmetry we use the polar angle θ formed by the direction of the outgoing photons with respect to the z -axis. We define the variable $\mu \equiv \cos \theta$ to report to present our results. Computing the spectra for photons in a narrow range of μ is equivalent to having a line-of-sight oriented in that direction.

$$v_z = 0, \quad (2.3)$$

where R is the radius of the sphere and V_{\max} is the linear velocity at the sphere's surface. The minus/plus sign in the x/y -component of the velocity indicates the direction of rotation. In this case we take the angular velocity in the same direction as the \hat{k} unit vector. With these definitions we can write the norm of the angular velocity as $\omega = V_{\max}/R$. For each photon in the simulation we have its initial position inside the sphere, direction of propagation \hat{k}_{in} and reduced frequency x_{in} . The photon's propagation stops once they cross the surface of the sphere. At this point we store the position, the outgoing direction of propagation \hat{k}_{out} and the reduced frequency x_{out} . We now define the angle θ by $\cos \theta = \hat{k}_{\text{out}} \cdot \hat{k} \equiv \mu$, it is the angle of the outgoing photons with respect to the direction of the angular velocity. We use the variable μ to study the anisotropy induced by rotation. Fig. 2.1 shows the geometry of the problem and the important variables.

2.0.2 Brief Description of the Radiative Transfer Codes

Here we briefly describe the relevant characteristics of the two radiative transfer codes we have used. For a detailed description we refer the reader to the original papers [25] and [32]. The codes follow the individual scatterings of Ly α photons as they travel through a 3D distribution of neutral Hydrogen. The frequency of the photon (in the laboratory frame) and its direction of propagation change at every scattering. This change in frequency is due to the peculiar velocities of the Hydrogen absorbing and re-emitting the photon. Once the photons escape the gas distribution we store their direction of

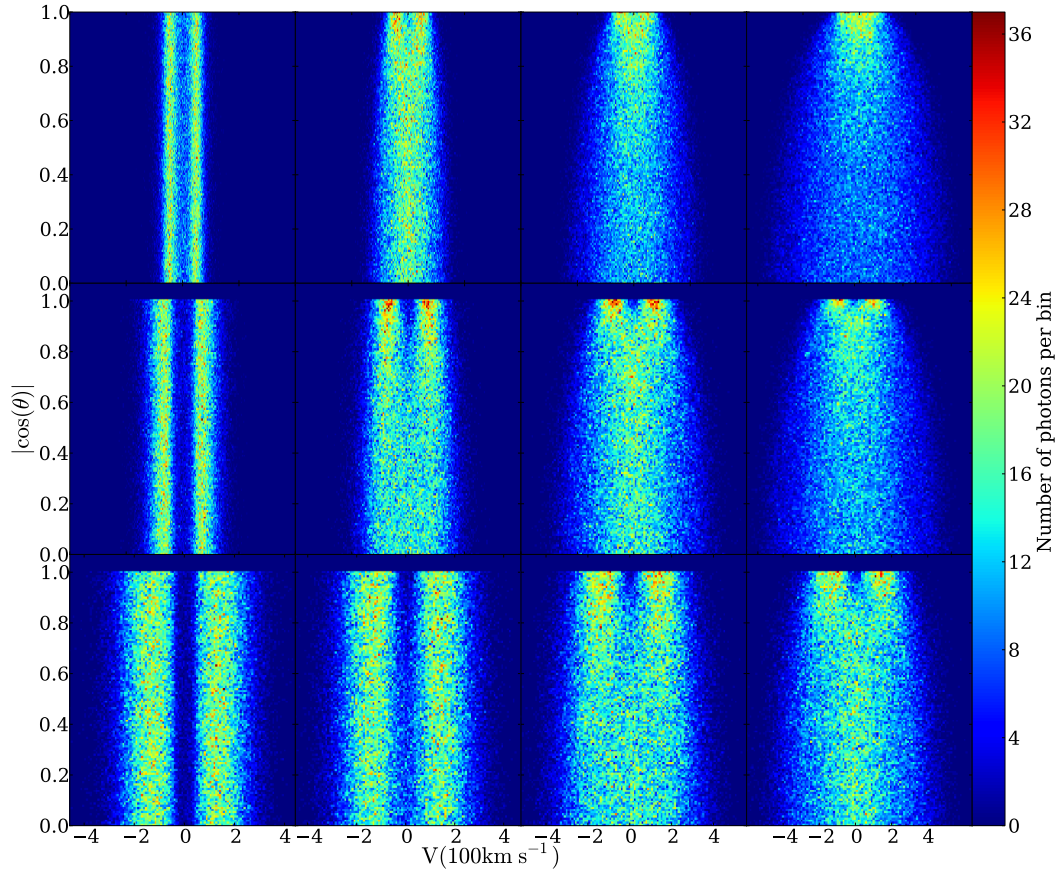


FIGURE 2.2: 2D histogram showing the number of photons that escape with frequency x forming an angle θ (parametrized as $|\cos \theta|$) with the rotation axis. The rotational velocity ($0, 100, 200, 300 \text{ km s}^{-1}$) increases from left to right and the optical depth ($10^5, 10^6, 10^7$) from top to bottom. The Ly α photons are initialized at the center of the sphere. Two main results can be read from this figure. First, the line morphology depends on the viewing angle. Second, the line can become single peaked for high rotational velocities.

propagation and frequency at their last scattering. The initialization process for the Ly α photons specifies its position, frequency and direction of propagation. We select the initial frequency to be exactly the Ly α rest-frame frequency in the gas reference frame and the direction of propagation to be random following a flat probability distribution over the sphere. It means that for photons emitted from the center of the sphere $x_{\text{in}} = 0$, while photons emitted at some radii with a peculiar velocity \vec{v} have initial values x_{in} depending on its direction of propagation: $x_{\text{in}} = \vec{v} \cdot \hat{k}_{\text{in}} / v_{\text{th}}$. We do not include the effect of turbulent velocities in the initialization. We neglect this given that the induced perturbation should be on the close to the thermal velocity, 12.8 km s^{-1} , which is one order of magnitude smaller than the velocity widths ($100\text{-}500 \text{ km s}^{-1}$) in the static case. If dust is present, the photon can interact either with a Hydrogen atom or dust grain. In the case of a dust interaction the photon can be either absorbed or scattered. This probability is encoded in the dust albedo, A , which we chose to be $1/2$. In order to

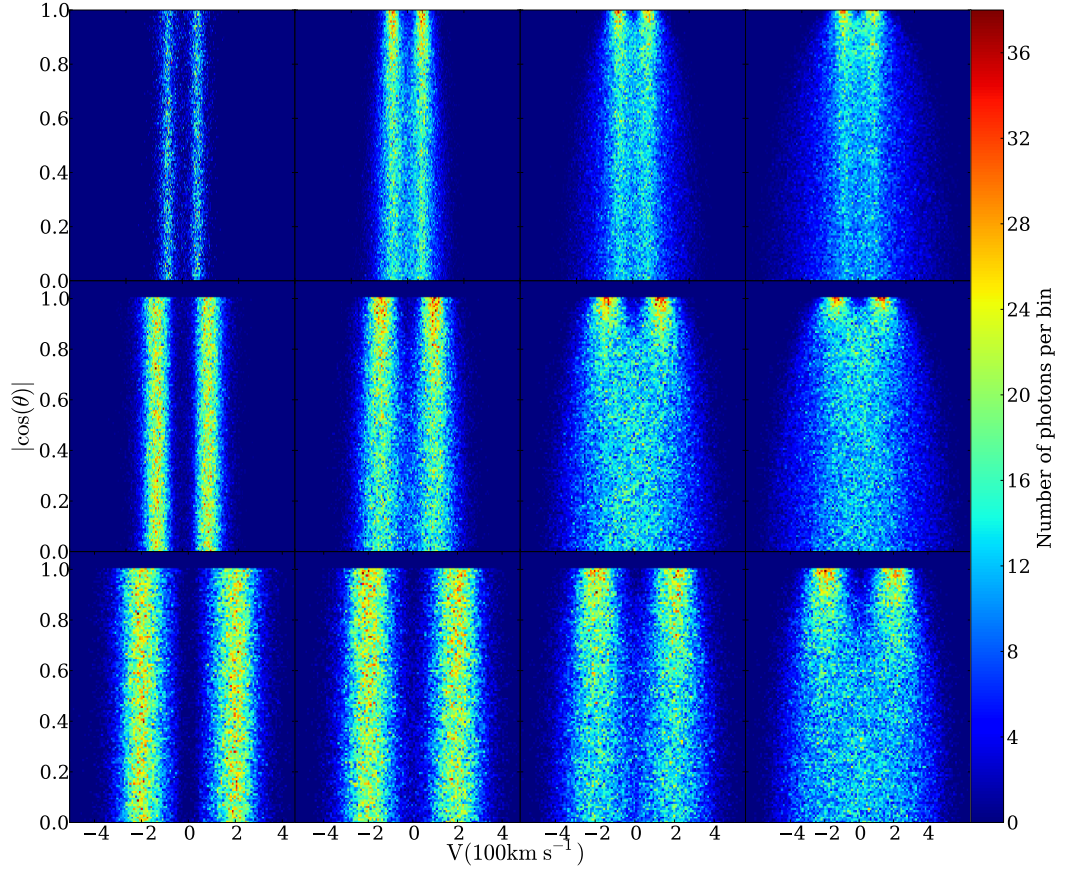


FIGURE 2.3: Same as Fig. 2.2 for Ly α photons initialized homogeneously throughout the sphere.

obtain accurate values for the escape fraction of photons in the presence of dust, we do not use any accelerating mechanism in the radiative transfer. The codes treat the gas as homogeneous in density and temperature. This implies that the gas is completely defined by its geometry (i.e. sphere or slab), temperature T , Hydrogen optical depth τ_H , dust optical depth τ_a and the bulk velocity field \vec{v} .

2.0.3 Grid of Simulated Galaxies

In the Monte Carlo calculations we follow the propagation of $N_\gamma = 10^5$ numerical photons through different spherical galaxies. For each galaxy we vary at least one of the following parameters: the maximum rotational velocity V_{\max} , the hydrogen optical depth τ_H , the dust optical depth τ_a and the initial distribution of photons with respect to the gas. In total there are 48 different models combining all the possible different variations in the input parameters. Table 2.1 lists the different parameters we used to generate the models. The results and trends we report are observed in both Monte Carlo codes.

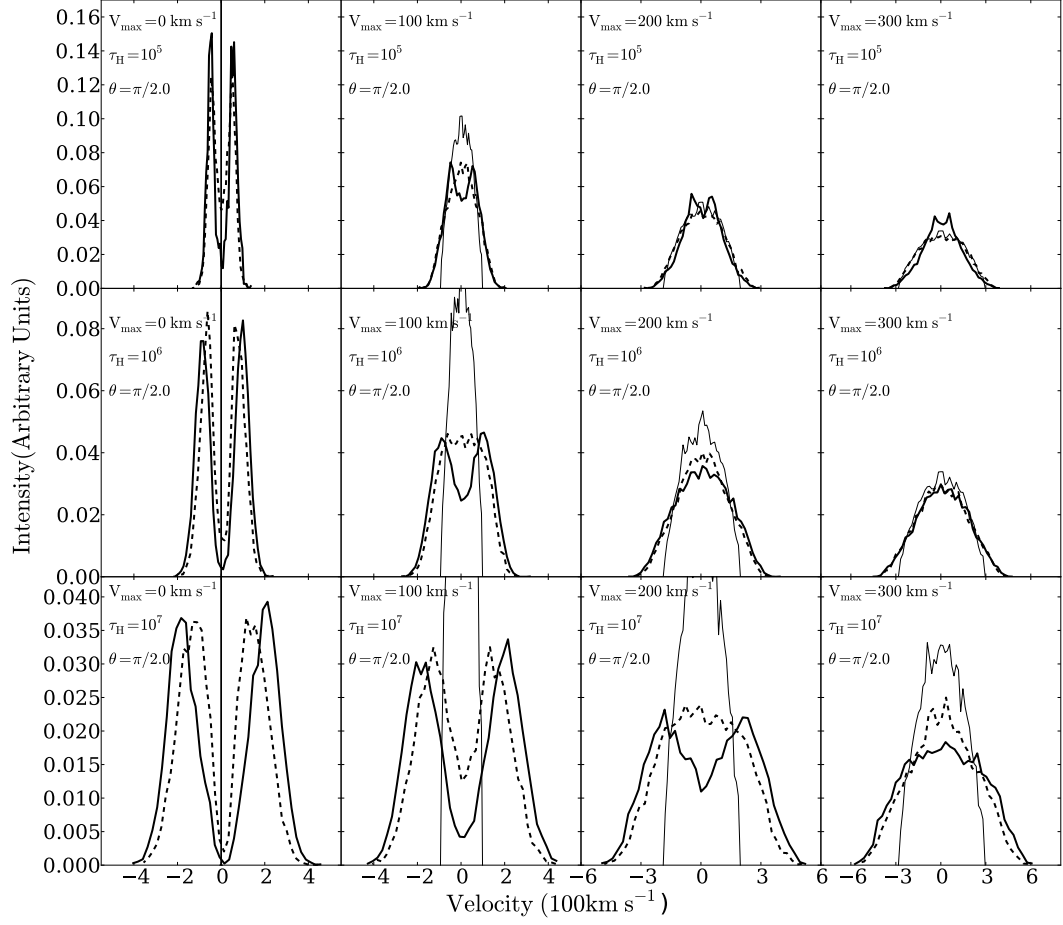


FIGURE 2.4: Shape of the Ly α line for different maximum rotational velocities for a LoS perpendicular to the rotation axis ($|\mu| \sim 0$). The continuous (dashed) line represents the central (homogeneous) source distributions. The continuous thin line represents the intrinsic homogeneous spectrum. The panels follow the same distribution as in Figs 2.2 and 2.3.

Physical Parameter (units)	Symbol	Values
Velocity (km s^{-1})	V_{max}	0, 100, 200, 300
Hydrogen Optical Depth	τ_H	10^5 , 10^6 , 10^7
Dust Optical Depth	τ_a	0,1
Photons Distributions		Central, Homogeneous

TABLE 2.1: Summary of Physical Parameters of our Monte Carlo Simulations.

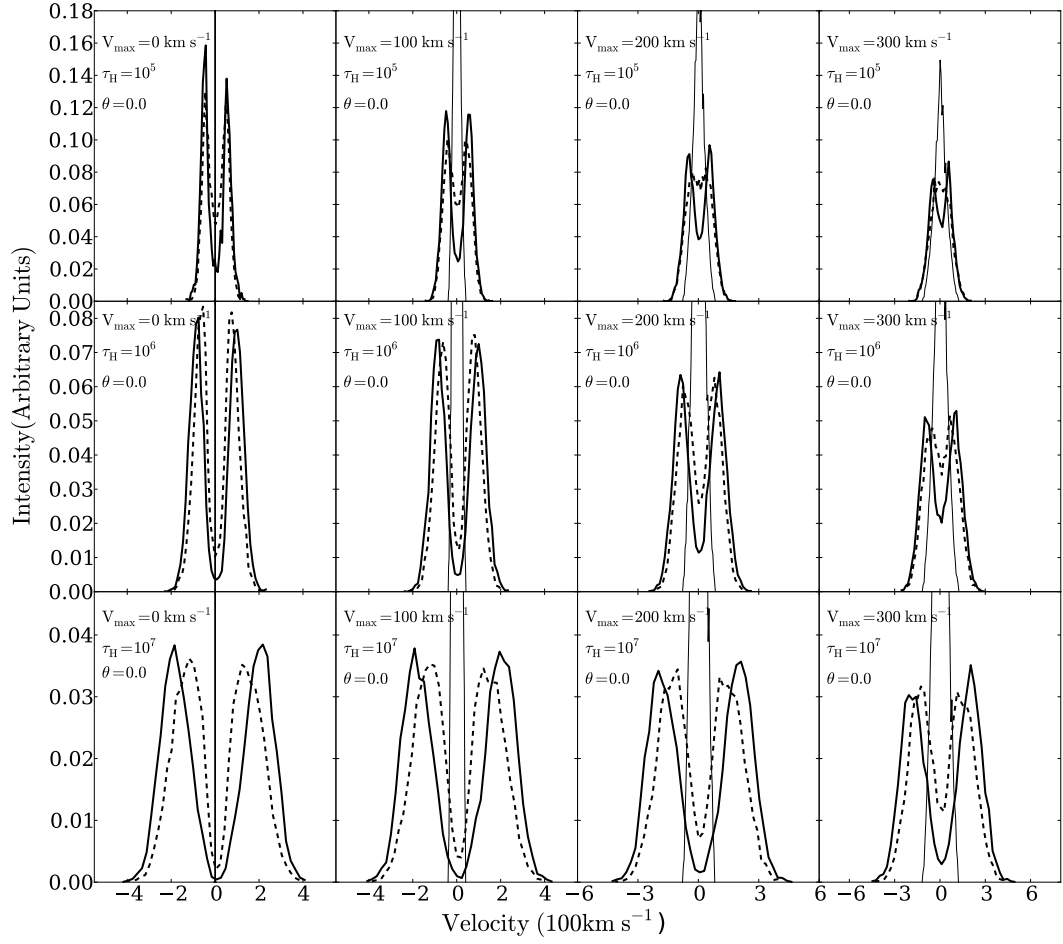


FIGURE 2.5: Shape of the Ly α line for different maximum rotational velocities for a LoS perpendicular to the rotation axis ($|\mu| \sim 1$). The continuous (dashed) line represents the central (homogeneous) source distributions. The continuous thin line represent the intrinsic homogeneous spectrum. The panels follow the same distribution as in Figs 2.2 and 2.3.

Chapter 3

Results

The main results of this thesis are summarized in Fig. 2.2 and 2.3. They show 2D histograms of the escape frequency x and outgoing angle θ parametrized by $|\mu|$. Taking into account only photons around a value of $|\mu|$ gives us the emission detected by an observer located at an angle θ with respect to the rotation axis. We have verified that the solutions are indeed symmetric with respect to $\mu = 0$. We have also verified that the total flux is the same for all μ . From these figures we can see that the line properties change with rotational velocity and depend on the viewing angle θ . In the next subsections we quantify the morphology changes with velocity, optical depth and viewing angle. We characterize the line morphology by its total intensity, the full width at half maximum, (FWHM) and the location of the peak maxima. In order to interpret the morphological changes in the line we also report the median number of scatter for each Ly α photon in the simulation. For the models where dust is included we measure the escape fraction as a function of rotational velocity and viewing angle.

3.0.4 Line Morphology

The first column in both Fig. 2.2 and 2.3 shows that for the static sphere the line properties are independent of $|\mu|$, as it is expected due to the spherical symmetry. However, for increasing rotational velocities, at a fixed optical depth, there are clear signs that this symmetry is broken. If the viewing angle is aligned with the rotation axis, $|\mu| \sim 1$, the Ly α line keeps a double peak with minor changes in the morphology as the rotational velocity increases. However, for a line of sight perpendicular to the rotation axis, $|\mu| \sim 0$, the impact of rotation is larger. The double peak readily transforms into a single peak. This is clear in Fig. 2.4 and in Fig. 2.5 where we present the different line morphologies for $|\mu| \sim 0$ and $|\mu| \sim 1$ for the homogeneous and central configurations. The panels have the same distribution as Fig. 2.2 and 2.3. There are three clear effects on the line

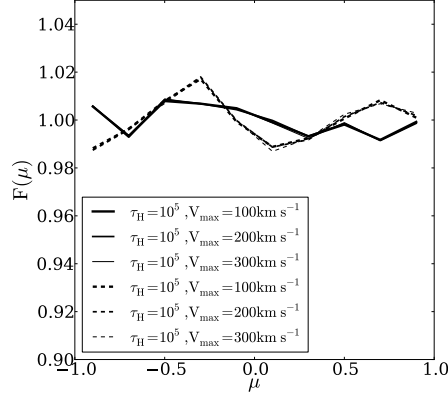


FIGURE 3.1: Integrated flux distribution as a function of the viewing angle as parametrized by μ . Continuous (dashed) correspond to central (homogeneous) source distribution. The models correspond to an optical depth of $\tau_H = 10^5$ and rotational velocities of 100 km s^{-1} , 200 km s^{-1} and 300 km s^{-1} . The distributions are flat in the range of models probed in this work, meaning that the integrated flux for all viewing angles is the same.

morphology as the rotational velocity increases. First, the line broadens; second, the double peaks reduce their intensity; and third, the intensity at the line centre rises. The last two effects are combined to give the impression that the double peaks are merged into a single one at high rotational velocities.

3.0.5 Integrated Line Intensity

We now consider possible variations in the integrated flux with respect to the viewing angle θ . To this end we define the normalized flux seen by an observer at an angle μ by:

$$F(\mu) = \frac{2\Delta N}{N\Delta\mu}, \quad (3.1)$$

where $\mu = \cos\theta$, N is the total number of outgoing photons, ΔN is the number of photons in an angular bin $\Delta\theta$. This definition satisfies the condition $\int_{-1}^1 F(\mu) d\mu/2 = 1$. In the case of perfect spherical symmetry one expects a flat distribution with $F(\mu) = 1$. Fig. 3.1 shows the results for a selection of models with $\tau_H = 10^5$, different rotational velocities and the two types of source distributions. This shows that $F(\mu)$ is consistent with being flat, apart from some statistical fluctuations on the order of 2%. This is a remarkable result: while the rotation axis defines preferential direction, the integrated flux is the same for all viewing angles in the range of parameters explored in this paper. This can be understood from the fact that *radiative transfer inside a sphere that undergoes solid-body rotation proceeds identical as inside a static sphere*: we can draw a line between any two atoms within the rotating cloud, and their relative velocity along this line is zero (apart from the relative velocity as a result of random thermal motion),

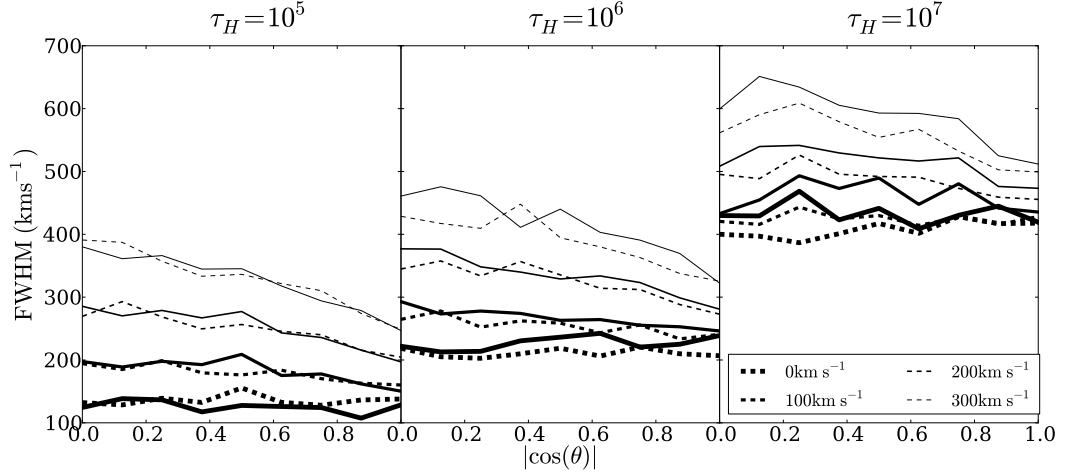


FIGURE 3.2: FWHM for the non-dusty models as a function of the viewing angle parametrized by $|\cos\theta|$. Continuous (dashed) lines correspond to central (homogeneous) source distributions. The general trend is of an decreasing line width as the line of sight becomes parallel to the rotation axis.

irrespective of the rotation velocity of the cloud. This relative velocity is what is relevant for the radiative transfer¹

3.0.6 Full Width at Half Maximum

We use the full width at half maximum (FWHM) to quantify the line broadening. We measure this width from the line intensity histogram by finding the values of the velocities at half maximum intensity. We use lineal interpolation between histogram points to get a value more precise than the bin size used to construct the histogram. Fig. 3.2 shows the FWHM for all models as a function of the viewing angle. The FWHM increases for decreasing values of μ (movement from the poles to the equator) and increasing values of V_{\max} . In Fig. 3.3 we fix $|\mu| < 0.1$, i.e. viewing angle perpendicular to the rotation axis, to plot the FWHM as a function of rotational velocity. We parametrize the dependency of the line width with V_{\max} as

$$\text{FWHM}^2 = \text{FWHM}_0^2 + V_{\max}^2/\lambda^2, \quad (3.2)$$

where FWHM_0 is the velocity width in the static case and λ is a positive scalar to be determined as a fit to the data. With this test we want to know to what extent the new velocity width can be expressed as a quadratic sum of the two relevant velocities in the

¹This point can be further illustrated by considering the path of individual photons: let a photon be emitted at line center ($x = 0$), in some random direction \mathbf{k} , propagate a distance that corresponds to $\tau_0 = 1$, scatter fully coherently (i.e. $x = 0$ after scattering in the gas frame) by 90° , and again propagate a distance that corresponds to $\tau_0 = 1$. The position where the photon scatters next does *not* depend on the rotation of the cloud, nor on \mathbf{k} .

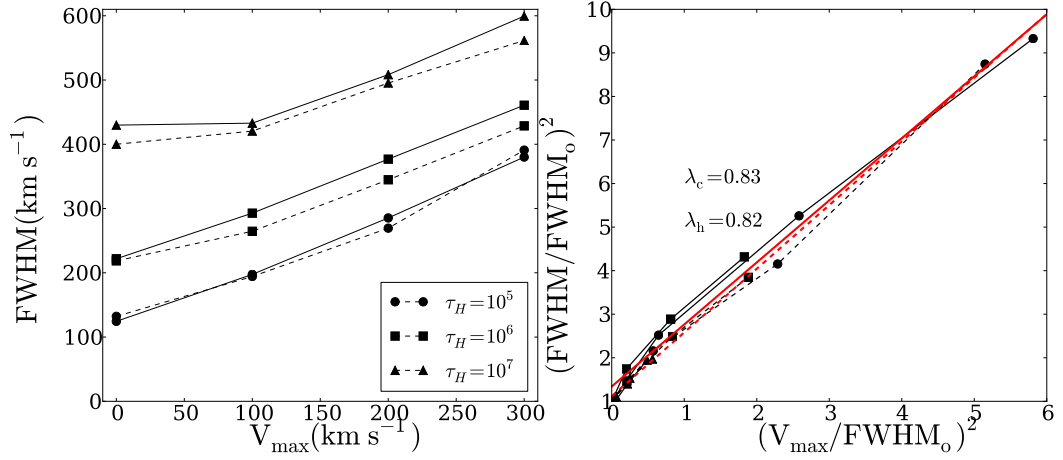


FIGURE 3.3: FWHM for the non-dusty models as a function of rotational velocity V_{max} for observers located perpendicular to the rotation axis. The left panel shows the results in velocity units while the right panel normalizes the data by the FWHM in the static case. Continuous (dashed) lines correspond to central (homogeneous) source distributions. The straight lines represent the fit to the data using the expression in Eq. (3.2).

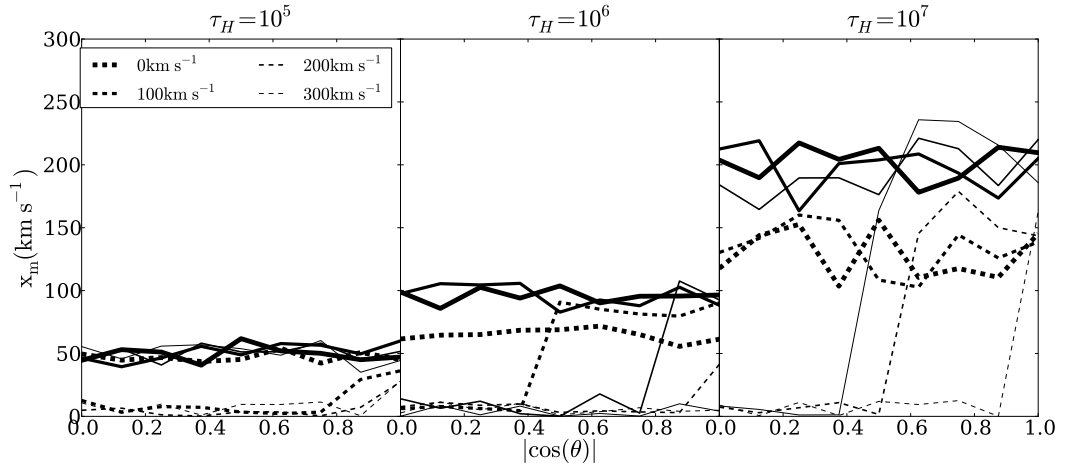


FIGURE 3.4: Position of the line maxima as a function of maximum rotational velocity V_{max} . Continuous (dashed) lines correspond to central (homogeneous) source distributions. A value of $x_{\text{max}} = 0$ indicates that line becomes single peaked.

problem. All the models fall into a single family of lines in the plane shown in the right panel of Fig. 3.3, justifying the choice of our parametrization. We fit simultaneously all the points in two separate groups, central and homogeneous sources. We find that these values are $\lambda_c = 0.83 \pm 0.06$ and $\lambda_h = 0.82 \pm 0.05$ respectively.

Source Distribution	τ_H	V_{\max} (km s ⁻¹)			
		0	100	200	300
Homogeneous	10 ⁵	0.263	0.263	0.263	0.263
	10 ⁶	0.291	0.292	0.293	0.293
	10 ⁷	0.228	0.228	0.228	0.228
Central	10 ⁵	0.096	0.096	0.096	0.096
	10 ⁶	0.066	0.066	0.066	0.066
	10 ⁷	0.015	0.016	0.016	0.015

TABLE 3.1: Escape fraction values for all dusty models.

3.0.7 Line Maxima

We measure the peak maxima position, x_m , to quantify the transition from double into single peak profiles. In Fig. 3.4 we show the dependence of x_m with the viewing angle parametrized by $|\cos\theta|$ for different rotational velocities. There are two interesting features that deserve attention. First, for a viewing angle parallel to the rotational axis ($\mu \sim 1.0$) the maxima of all models with the same kind of source initialization are similar regardless of the rotational velocity. Second, at a viewing angle perpendicular to the rotation axis ($\mu \sim 0.0$) a large fraction of models become single peaked. This feature appears more frequently for homogeneously distributed sources if all the other parameters are equal.

3.0.8 Dusty Clouds: Escape Fraction

We now estimate the escape fraction f_{esc} for the dusty models. The main result is that we do not find any significant dependence with either the viewing angle nor the rotational velocity. This is consistent with our finding in § 3.0.5, that radiative transfer inside the cloud does not depend on its rotational velocity. For completeness we list in Table 3.1 the escape fraction for all models. We now put these results in the context of the analytic solution for the infinite slab[11]. In Neufeld's set-up the analytic solution depends uniquely on the product $(a\tau_H)^{1/3}\tau_A$ where $\tau_A = (1 - A)\tau_a$, valid only in the limit $a\tau_H \gg 1$. At fixed values of τ_a the escape fraction monotonically decreases with increasing values of τ_H . This expectation holds for the central sources. But in the case of homogeneous sources the escape fraction increases slightly from $\tau_H = 10^5$ to $\tau_H = 10^6$. The naive interpretation of the analytic solution does not seem to hold for photons emitted far from the sphere's center. We suggest that increasing τ_H from 10^5 to 10^6 causes a transition from the 'optically thick' to the 'extremely optically thick' regime for a noticeable fraction of the photons in the homogeneous source distribution. In the

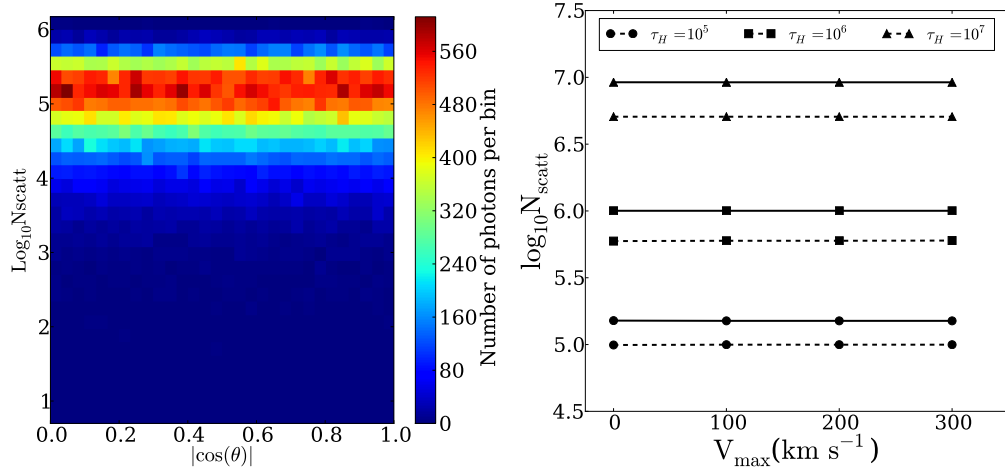


FIGURE 3.5: 2D histogram of the logarithm of the average number of scatterings as function of μ (left) and the maximum rotational velocity V_{max} (right). The left panel shows the behaviour for $\tau = 10^5$ and $V_{\text{max}} = 300 \text{ km s}^{-1}$ as a function of $|\cos \theta|$, the color indicates the number of photons per bin. In the right panel the continuous (dashed) lines represent the results for the central (homogeneous) model. The independence of N_{scatt} with μ and V_{max} is present in all models.

optically thick regime, Ly α photons can escape in 'single flight' which corresponds to a scenario in which the photon resonantly scatters $10^4 - 10^5$ times until it is scattered into the wing of the line ($x \sim 3 - 4$). At these frequencies the medium is optically thin, and the photons can escape efficiently in a single flight. In contrast, in an extremely optically thick medium Ly α photons escape in a 'single excursion' [9]. Here, photons that are scattered into the wing of the line escape from the medium in a sequence of wing scattering events. In both cases, Ly α photons resonantly scatter 10^4 - 10^5 times. Because we keep our clouds the same size, the mean free path of Ly α photons that scatter resonantly is 10 times larger for the case $\tau_H = 10^5$ than for $\tau_H = 10^6$. If we compute the average distance D travelled by Ly α photons through a medium of size R as a function of line center optical depth τ_H , then we find that during the transition from optically thick to extremely optically thick the mean traversed distance D actually decreases slightly. This decrease is unique to this transition region, and D generally increases with τ_H at other values of τ_H .

3.0.9 Average Number of Scatterings

The number of scatterings affects the escape frequency of a Ly α photon. Studying this quantity further illustrates the independence of the integrated flux and the escape fraction on rotational velocity. In Fig. 3.5 we show the average number of scatterings $\langle N_{\text{scatt}} \rangle$ as a function of the cosine of the outgoing angle $|\cos \theta|$ and the rotational velocity V_{max} . From the right panel observe that the number of scatterings and the

outgoing angle are independent. This plot corresponds to the specific case of the central model with $\tau = 10^5$ and $V_{\text{max}} = 300 \text{ km s}^{-1}$, but we have verified that this holds for all models. The right panel of Fig. 3.5 shows how the average number of scatterings is also independent from the rotational velocity. The lower number of average scatterings in the homogeneous source distribution is due to a purely geometrical effect. Photons emitted close to the surface go through less scatterings before escaping. In static configurations it is expected that the optical depth correlates number of scatterings. This has been precisely quantified in the case of static infinite slab. In that model for centrally emitted sources the average number of scatterings depends only on the optical depth $\langle N_{\text{scatt}} \rangle = 1.612\tau_{\text{H}}$ [9, 10], for homogeneously distributed sources $\langle N_{\text{scatt}} \rangle = 1.16\tau_{\text{H}}$ [10]. In our case we find that for the central model the number of scatterings is proportional to the optical depth, with $\langle N_{\text{scatt}} \rangle = (1.50, 1.00, 0.92)\tau_{\text{H}}$ for optical depth values of $\tau_{\text{H}} = (10^5, 10^6, 10^7)$ respectively. For the homogeneous sources we find that $\langle N_{\text{scatt}} \rangle = (0.99, 0.59, 0.51)\tau_{\text{H}}$.

Chapter 4

Discussion

4.0.10 Towards an analytical description

There is a key result of our simulations that allows us to build an analytical description for the outgoing spectra. It is the independence of the following three quantities with the rotational velocity and the viewing angle: integrated flux, average number of scatterings and escape fraction. As we explained in § 3.0.5, the best way to understand this is that radiative transfer inside a sphere that undergoes solid-body rotation proceeds identical to that inside a non-rotating sphere. While scattering events off atoms within the rotating cloud impart Doppler boosts on the Ly α photon, these Doppler boost are only there in the lab-frame. Therefore, in the frame of the rotating gas cloud all atoms are stationary with respect to each other and the scattering process proceeds identical as in the static case (also see § 3.0.5 for an additional more quantitative explanation). This result allows us to analytically estimate the spectrum emerging from a rotating cloud: The spectrum of Lyman α photons emerging from a rotating gas cloud is identical as for the static case in a frame that is co-rotating with the cloud. However, the surface of cloud now moves in the lab-frame. Each surface-element on the rotating cloud now has a bulk velocity with respect to a distant observer. In order to compute the spectrum one can integrate over all the surface elements in the sphere with their corresponding shift in velocity and an additional weight by the surface intensity. Fig 4.1 shows some examples of analytic versus full MC spectra using this approach (the implementation details are in the Appendix). The left panel shows the results for different rotational velocities in the case of $\tau_H = 10^7$ and an observer located perpendicular to the axis of rotation ($i = 0$ in the scheme of Fig A.1 in the Appendix). The right panel shows the results for different viewing angles in the case of $\tau_H = 10^7$ and a rotational velocity of $V_{\max} = 300 \text{ km s}^{-1}$. The two methods clearly give good agreement, though not perfect. In particular, the left panel shows that the MC gives rise to a spectrum that is slightly

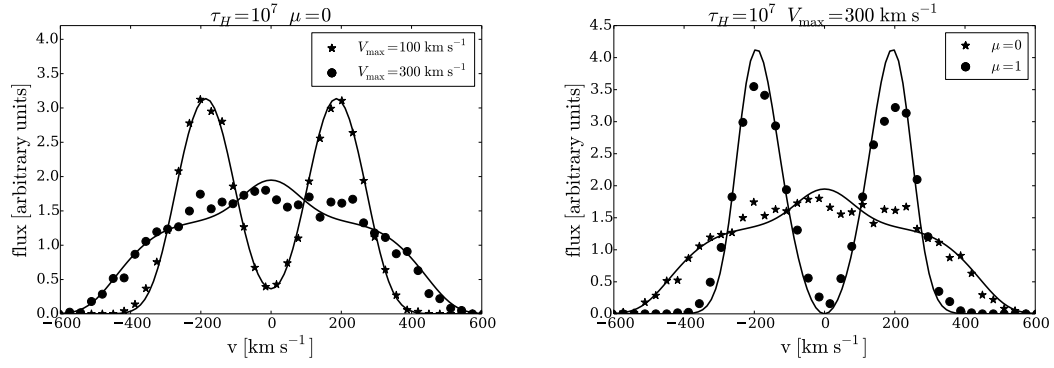


FIGURE 4.1: Comparison of the Monte Carlo results against the analytic solution. The left panel explores the results of different velocities. The right panel presents the results for two different observers: paralel and perpendicular to the rotational axis, $\mu = 1$ and $\mu = 0$ respectively.

more concentrated towards the line centre. As we explain in Appendix A, we do not expect perfect agreement, because this requires an analytic solution for the spectrum of Ly α photons emerging from a static, optically extremely thick cloud *as a function of the angle at which they escape from the sphere*. This solution does not exist in the literature. It is possible to get better agreement by modifying the surface brightness profile. In any case, the analytic calculation closely captures the results obtained from the full calculations from the MC simulations. As such, they are extremely useful and provide us with a quick tool to verify our calculations at the first order level.

4.0.11 Impact on the interpretation of simulated and observational data

We now compare our findings to other computational results and discuss its possible implications for the interpretation of observational data. **Escape at Line Center.** Our models have shown that rotation enhances the flux density at line center (see Fig. 2.4). It has recently been proposed that galaxies with Ly α spectral lines that contain flux at line center may be ‘leaking’ ionizing (LyC) photons [34?]. The main reason for this possible connection is that the escape of ionizing (LyC) photons requires $N_{\text{HI}} < 10^{17} \text{ cm}^{-2}$. The same low column densities facilitate the escape of Ly α photons at (or close to) line center. Our work suggests that rotation may provide an alternative explanation. **Single peaked lines.** The presence of single peaked profiles has been associated to inflow/outflow dynamics [21, 32]. Gas bulk rotation can also be considered as a probable origin for that behaviour, provided that the observed single peak is highly symmetric. Similarly, in the case of double peaked lines with a high level of flux at the line center, rotation also deserves to be considered in the pool of possible bulk flows responsible for that feature,

specially if the two peaks have similar intensities. **Systemic velocities.** There are observational measurements for the velocity shift between the Ly α and other emission lines. In our study we find that the position of the peak maxima can suddenly change with rotation and viewing angle. Namely the line can become single peaked for high rotational velocities and viewing angles perpendicular to the rotation axis. **Galaxy simulations with gas rotation.** [30] studied Ly α line emission in two high resolution simulations of individual galaxies. The main purpose of their study was to assess the impact of two different ISM prescriptions. However, each simulated galaxy had a disc structure with a clear rotation pattern in the ISM and inflowing gas from the circumgalactic region. The configuration had an axial symmetry and they reported a strong dependence of both the escape fraction and the total line intensity as a function of the θ angle. From our study, none of these two quantities has a dependence either on the inclination angle or the rotational velocity. We suggest that the effect reported by [30] is consistent with being a consequence of the different hydrogen optical depth for different viewing angles and not as an effect of the bulk rotation. **Zero impact on the Ly α escape fraction.** Study of high redshift LAEs in numerical simulation often requires the estimation of the Ly α escape fraction in order to compare their results against observations [23? –26]. Most of these models estimate the escape fraction from the column density of dust and neutral Hydrogen. The results of our simulation indicate that the rotational velocity does not induce additional uncertainties in those estimates.

Chapter 5

Conclusions

In this work we quantified for the first time in the literature the effects of gas bulk rotation in the morphology of the Ly α emission line in star forming galaxies. Our results are based on the study of an homogeneous sphere of gas with solid body rotation. We explore a range of models by varying the rotational speed, hydrogen optical depth, dust optical depth and initial distribution of Ly α photons with respect to the gas density. As a cross-validation, we obtained our results from two independently developed Monte-Carlo radiative transfer codes. Two conclusions stand out from our study. First, rotation clearly impacts the Ly α line morphology; the width and the relative intensity of the center of the line and its peaks are affected. Second, rotation introduces an anisotropy for different viewing angles. For viewing angles close to the poles the line is double peaked and it makes a transition to a single peaked line for high rotational velocities and viewing angles along the equator. This trend is clearer for spheres with homogeneously distributed radiation sources than it is for central sources. Remarkably, we find three quantities that are invariant with respect to the viewing angle and the rotational velocity: the integrated flux, the escape fraction and the average number of scatterings. These results helped us to construct the outgoing spectra of a rotating sphere as a superposition of spectra coming from a static configuration. This description is useful to describe the main quantitative features of the Monte Carlo simulations. Quantitatively, the main results of our study are summarized as follows.

- In all of our models, rotation induces changes in the line morphology for different values of the angle between the rotation axis and the LoS, θ . The changes are such that for a viewing angle perpendicular to the rotation axis, and high rotational velocities the line becomes single peaked.
- The line width increases with rotational velocity. For a viewing angle perpendicular to the rotation axis This change approximately follows the functional form

$\text{FWHM}^2 = \text{FWHM}_0^2 + (V_{\text{max}}/\lambda)^2$, where FWHM_0 indicates the line width for the static case and λ is a constant. We have determined this constant to be $\lambda_c = 0.83 \pm 0.06$ and $\lambda_h = 0.82 \pm 0.05$ for the central and homogeneous source distributions, respectively.

- At fixed rotational velocity the line width decreases as $|\mu|$ increases, i.e. the smallest value of the line width is observed for a line of sight parallel to the rotation axis.
- The single peaked line emerges at viewing angles $\mu \sim 1$ for when the rotational velocity is close to than half the FWHM_0 .

Comparing our results with recent observed LAEs we find that morphological features such as high central line flux, single peak profiles could be explained by gas bulk rotation present in these LAEs. The definitive and clear impact of rotation on the $\text{Ly}\alpha$ morphology suggests that this is an effect that should be taken into account at the moment of interpreting high resolution spectroscopic data. In particular it is relevant to consider the joint effect of rotation and ubiquitous outflows (M.C. Remolina-Gutierrez et al., in prep.) because rotation can lead to enhanced escape of $\text{Ly}\alpha$ at line center, which has also been associated with escape of ionizing (LyC) photons [34?]

Appendix A

Analytic Expression for the $\text{Ly}\alpha$ Spectrum emerging from Rotating Cloud

$\text{Ly}\alpha$ scattering through an optically thick gas cloud that is undergoing solid-body rotation (i.e. in which the angular speed around the rotation axis is identical for each hydrogen atom) proceeds identical as in a static cloud. In order to compute the spectrum emerging from a rotating cloud, we sum the spectra emerging from all surface elements of the cloud, weighted by their intensity. We adopt the geometry shown in Fig A.1 to derive an analytic expression of this emerging spectrum, Note that this geometry differs from the scheme shown in Fig 1 in the main body of the thesis. The

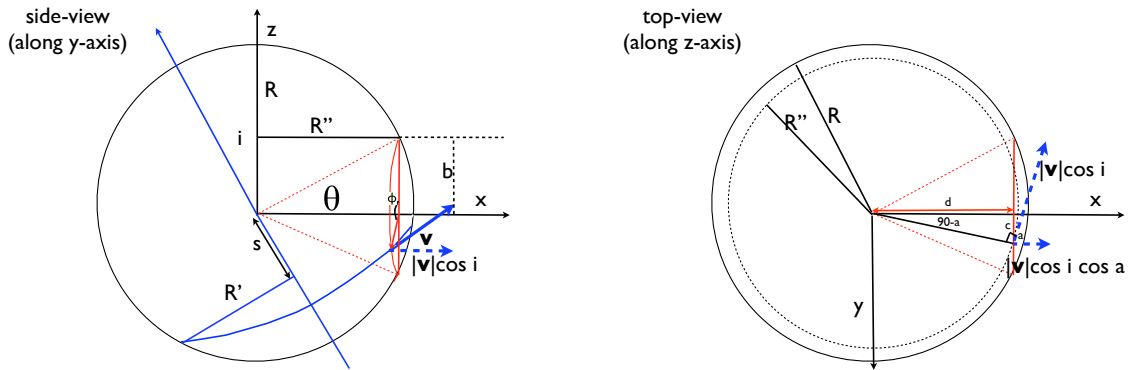


FIGURE A.1: Adopted geometry for evaluating the analytic spectrum.

sightline to the observer & rotation axis define the $x - z$ plane. The *left panel* in Fig A.1 shows the view from the y -axis. The observer sits along the x axis. The rotation axis makes an angle i with respect to the z -axis. We sum up spectra from individual patches

by integrating over the impact parameter b , and angle ϕ . Each (b, ϕ) corresponds to a point on the sphere. This point has a velocity vector $\mathbf{v}(b, \phi, i)$, which we denote with \mathbf{v} for brevity. The magnitude of \mathbf{v} is $|\mathbf{v}| = V_{\max} R'/R$. Here $R' = \sqrt{R^2 - s^2}$, in which s denotes the distance of the point (b, ϕ) to the plane perpendicular to the rotation axis and through the origin (see the *left panel* of Fig A.1). This distance s is given by $s = |-\sin i \sqrt{R^2 - b^2} + b \cos \phi \cos i|$.

The spectrum of the flux emerging from the surface at point (b, ϕ) is

$$J(x, b, \phi, i) = \frac{\sqrt{\pi}}{\sqrt{24}a\tau_0} \left(\frac{(x - x_b)^2}{1 + \cosh \left[\sqrt{\frac{2\pi^3}{27}} \frac{|(x - x_b)^3|}{a\tau_0} \right]} \right),$$

where $x_b \equiv v_b/v_{\text{th}}$, and v_b is the component of \mathbf{v} projected onto the line-of-sight. This component is given by

$$v_b(b, \phi, i) = V_{\max} \frac{\sqrt{R^2 - s^2}}{R} \cos i \cos a, \quad (\text{A.1})$$

where $\beta = 90^\circ - a$. The factor $\cos i$ accounts for the projection onto the $x - y$ plane, and the factor $\cos a$ for the subsequent projection onto the line-of-sight. The *right panel* of Fig. A.1 shows that this angle a can be computed from

$$\tan \beta = \tan[90^\circ - a] = \frac{c}{d} = \frac{b \sin \phi}{\sqrt{R^2 - b^2}}, \quad (\text{A.2})$$

In order to compute the total intensity we integrate over b and ϕ with a weight given by the surface brightness of the sphere at (b, ϕ) , $S(b, \phi)$.

$$J(x, i) = 2\pi \int_0^R db b \int_0^{2\pi} d\phi S(b, \phi) J(x, b, \phi, i) \approx 2\pi \int_0^R db b \int_0^{2\pi} d\phi J(x, b, \phi, i).$$

In the last expression we assume that $S(b, \phi)$ is constant. This corresponds to $I(\mu) \propto \mu$ at the surface, where μ denotes the cosine of the angle of the propagation direction of the outgoing photon and the normal to the sphere's surface: a fixed db corresponds to a physical length $ds = db/\mu$ on the sphere. If $I(\mu)$ were constant, this would imply that the sphere should appear brighter per unit b . A constant surface brightness profile requires the directional dependence for $I(\mu) \propto \mu$ to correct for this. Indeed, this is what is expected for the escape of Ly α photons from static, extremely opaque media (see Ahn et al. [17]; their Fig 4 and accompanying discussion). It is worth stressing that this derivation should not be viewed as a complete analytic calculation, and we do not expect perfect agreement: we *assumed* a functional form for the surface brightness profile [or for $I(\mu)$]. Moreover, $I(\mu)$ itself may depend on frequency x . In other words, analytic solutions exist for $J(x) = \int_0^1 I(x, \mu) d\mu$ at the boundary of the sphere, and *approximate* expressions for $I(\mu) = \int dx I(x, \mu)$, but *not* for $I(x, \mu)$ itself. The spectra we obtained

from the Monte-Carlo calculations naturally include the proper $I(x, \mu)$, and are therefore expected to be more accurate. To further test the assumption of scattering in a rotating medium proceeding as in a static medium we compute the distribution of the outgoing angles μ . The results are shown in Figure A.2; it shows that the distribution for μ is independent of the rotational velocity and the location over the sphere. The only dependence comes with τ_H . For higher values of the optical depth the distribution gets closer to $I(\mu) \propto \mu$ as expected for a static medium [17].

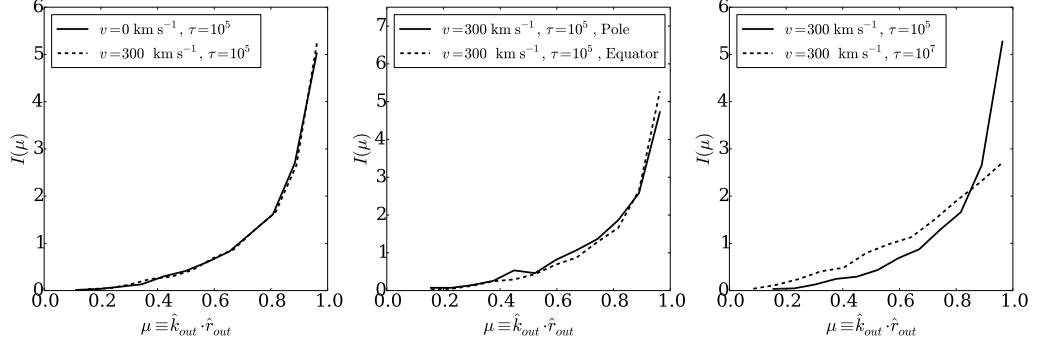


FIGURE A.2: Distribution of the cosine of the angle between the propagation direction and a vector normal to the sphere's surface. The distributions have been normalized to unity. Left panel: different rotational velocities; middle panel: different viewing angles; right panel: different optical depths. Only the optical depth has an effect on the distribution of outgoing directions. This is consistent with the assumption that Lyman α scattering in a medium with solid body rotation proceeds as in a static medium.

Bibliography

- [1] R. B. Partridge and P. J. E. Peebles. Are Young Galaxies Visible? *ApJ*, 147:868, March 1967. doi: 10.1086/149079.
- [2] J. E. Rhoads, S. Malhotra, A. Dey, D. Stern, H. Spinrad, and B. T. Jannuzi. First Results from the Large-Area Lyman Alpha Survey. *ApJ*, 545:L85–L88, December 2000. doi: 10.1086/317874.
- [3] E. Gawiser, H. Francke, K. Lai, K. Schawinski, C. Gronwall, R. Ciardullo, R. Quadri, A. Orsi, L. F. Barrientos, G. A. Blanc, G. Fazio, and J. J. Feldmeier. Ly α -Emitting Galaxies at $z = 3.1$: L* Progenitors Experiencing Rapid Star Formation. *ApJ*, 671:278–284, December 2007. doi: 10.1086/522955.
- [4] R. S. Koehler, P. Schuecker, and K. Gebhardt. Probing dark energy with baryonic acoustic oscillations at high redshifts. *aap*, 462:7–20, January 2007. doi: 10.1051/0004-6361:20065649.
- [5] M. Ouchi, K. Shimasaku, M. Akiyama, C. Simpson, T. Saito, Y. Ueda, H. Furusawa, K. Sekiguchi, T. Yamada, T. Kodama, N. Kashikawa, S. Okamura, M. Iye, T. Takata, M. Yoshida, and M. Yoshida. The Subaru/XMM-Newton Deep Survey (SXDS). IV. Evolution of Ly α Emitters from $z=3.1$ to 5.7 in the 1 deg² Field: Luminosity Functions and AGN. *ApJs*, 176:301–330, June 2008. doi: 10.1086/527673.
- [6] T. Yamada, Y. Nakamura, Y. Matsuda, T. Hayashino, R. Yamauchi, N. Morimoto, K. Kousai, and M. Umemura. Panoramic Survey of Ly α Emitters at $z = 3.1$. *Aj*, 143:79, April 2012. doi: 10.1088/0004-6256/143/4/79.
- [7] M. A. Schenker, D. P. Stark, R. S. Ellis, B. E. Robertson, J. S. Dunlop, R. J. McLure, J.-P. Kneib, and J. Richard. Keck Spectroscopy of Faint $3 < z < 8$ Lyman Break Galaxies: Evidence for a Declining Fraction of Emission Line Sources in the Redshift Range $6 < z < 8$. *ApJ*, 744:179, January 2012. doi: 10.1088/0004-637X/744/2/179.
- [8] S. L. Finkelstein, C. Papovich, M. Dickinson, M. Song, V. Tilvi, a. M. Koekoer, K. D. Finkelstein, B. Mobasher, H. C. Ferguson, M. Giavalisco, N. Reddy,

- M. L. N. Ashby, a. Dekel, G. G. Fazio, a. Fontana, N. a. Grogin, J.-S. Huang, D. Kocevski, M. Rafelski, B. J. Weiner, and S. P. Willner. A galaxy rapidly forming stars 700 million years after the Big Bang at redshift 7.51. *Nature*, 502 (7472):524–527, October 2013. ISSN 0028-0836. doi: 10.1038/nature12657. URL <http://www.nature.com/doifinder/10.1038/nature12657>.
- [9] T. F. Adams. The Escape of Resonance-Line Radiation from Extremely Opaque Media. *ApJ*, 174:439, June 1972. doi: 10.1086/151503.
- [10] J. P. Harrington. The scattering of resonance-line radiation in the limit of large optical depth. *MNRAS*, 162:43, 1973.
- [11] D. A. Neufeld. The transfer of resonance-line radiation in static astrophysical media. *ApJ*, 350:216–241, February 1990. doi: 10.1086/168375.
- [12] M. Dijkstra, Z. Haiman, and M. Spaans. Ly α Radiation from Collapsing Protogalaxies. I. Characteristics of the Emergent Spectrum. *ApJ*, 649:14–36, September 2006. doi: 10.1086/506243.
- [13] A. Loeb and G. B. Rybicki. Scattered Ly α Radiation around Sources before Cosmological Reionization. *ApJ*, 524:527–535, October 1999. doi: 10.1086/307844.
- [14] L. H. Auer. Transfer of Lyman Alpha in Diffuse Nebulae. *ApJ*, 153:783, September 1968. doi: 10.1086/149705.
- [15] L. W. Avery and L. L. House. An Investigation of Resonance-Line Scattering by the Monte Carlo Technique. *ApJ*, 152:493, May 1968. doi: 10.1086/149566.
- [16] S.-H. Ahn, H.-W. Lee, and H. M. Lee. Ly Alpha Transfer in a Thick, Dusty, and Static Medium. *Journal of Korean Astronomical Society*, 33:29–36, April 2000.
- [17] S.-H. Ahn, H.-W. Lee, and H. M. Lee. Ly α Line Formation in Starbursting Galaxies. I. Moderately Thick, Dustless, and Static H I Media. *ApJ*, 554:604–614, June 2001. doi: 10.1086/321374.
- [18] Z. Zheng and J. Miralda-Escudé. Monte Carlo Simulation of Ly α Scattering and Application to Damped Ly α Systems. *ApJ*, 578:33–42, October 2002. doi: 10.1086/342400.
- [19] M. Hansen and S. P. Oh. Lyman α radiative transfer in a multiphase medium. *MNRAS*, 367:979–1002, April 2006. doi: 10.1111/j.1365-2966.2005.09870.x.
- [20] S.-H. Ahn, H.-W. Lee, and H. M. Lee. P Cygni type Ly α from starburst galaxies. *MNRAS*, 340:863–869, April 2003. doi: 10.1046/j.1365-8711.2003.06353.x.

- [21] A. Verhamme, D. Schaerer, and A. Maselli. 3D Ly α radiation transfer. I. Understanding Ly α line profile morphologies. *AAP*, 460:397–413, December 2006. doi: 10.1051/0004-6361:20065554.
- [22] M. Dijkstra. Lyman Alpha Emitting Galaxies as a Probe of Reionization. *ArXiv e-prints*, arXiv:1406.7292, June 2014.
- [23] A. Orsi, C. G. Lacey, and C. M. Baugh. Can galactic outflows explain the properties of Ly α emitters? *MNRAS*, 425:87–115, September 2012. doi: 10.1111/j.1365-2966.2012.21396.x.
- [24] T. Garel, J. Blaizot, B. Guiderdoni, D. Schaerer, A. Verhamme, and M. Hayes. Modelling high redshift Lyman α emitters. *MNRAS*, 422:310–325, May 2012. doi: 10.1111/j.1365-2966.2012.20607.x.
- [25] J. E. Forero-Romero, G. Yepes, S. Gottlöber, S. R. Knollmann, A. J. Cuesta, and F. Prada. CLARA’s view on the escape fraction of Lyman α photons in high-redshift galaxies. *MNRAS*, 415:3666–3680, August 2011. doi: 10.1111/j.1365-2966.2011.18983.x.
- [26] J. E. Forero-Romero, G. Yepes, S. Gottlöber, and F. Prada. Modelling the fraction of Lyman break galaxies with strong Lyman α emission at $5 \leq z \leq 7$. *MNRAS*, 419:952–958, January 2012. doi: 10.1111/j.1365-2966.2011.19744.x.
- [27] C. Behrens and J. Niemeyer. Effects of Lyman-alpha scattering in the IGM on clustering statistics of Lyman-alpha emitters. *AAP*, 556:A5, August 2013. doi: 10.1051/0004-6361/201321172.
- [28] P. Laursen, J. Sommer-Larsen, and A. C. Andersen. Ly α Radiative Transfer with Dust: Escape Fractions from Simulated High-Redshift Galaxies. *ApJ*, 704:1640–1656, October 2009. doi: 10.1088/0004-637X/704/2/1640.
- [29] L. A. Barnes, M. G. Haehnelt, E. Tescari, and M. Viel. Galactic winds and extended Ly α emission from the host galaxies of high column density quasi-stellar object absorption systems. *MNRAS*, 416:1723–1738, September 2011. doi: 10.1111/j.1365-2966.2011.18789.x.
- [30] A. Verhamme, Y. Dubois, J. Blaizot, T. Garel, R. Bacon, J. Devriendt, B. Guiderdoni, and A. Slyz. Lyman- α emission properties of simulated galaxies: interstellar medium structure and inclination effects. *AAP*, 546:A111, October 2012. doi: 10.1051/0004-6361/201218783.
- [31] H. Yajima, Y. Li, Q. Zhu, T. Abel, C. Gronwall, and R. Ciardullo. Were Progenitors of Local L* Galaxies Ly α Emitters at High Redshift? *ApJ*, 754:118, August 2012. doi: 10.1088/0004-637X/754/2/118.

-
- [32] M. Dijkstra and R. Kramer. Line transfer through clumpy, large-scale outflows: Ly α absorption and haloes around star-forming galaxies. *MNRAS*, 424:1672–1693, August 2012. doi: 10.1111/j.1365-2966.2012.21131.x.
- [33] Z. Zheng and J. Wallace. Anisotropic Lyman-alpha Emission. *ArXiv e-prints*, August 2013.
- [34] C. Behrens, M. Dijkstra, and J. C. Niemeyer. Beamed Ly α emission through outflow-driven cavities. *AAP*, 563:A77, March 2014. doi: 10.1051/0004-6361/201322949.